



Efficient electrically powered CO₂-to-ethanol via suppression of deoxygenation

Xue Wang^{1,10}, Ziyun Wang^{1,10}, F. Pelayo García de Arquer¹, Cao-Thang Dinh¹, Adnan Ozden², Yuguang C. Li¹, Dae-Hyun Nam¹, Jun Li^{1,2}, Yi-Sheng Liu³, Joshua Wicks¹, Zitao Chen⁴, Miaofang Chi⁴, Bin Chen¹, Ying Wang¹, Jason Tam⁵, Jane Y. Howe⁵, Andrew Proppe^{1,6}, Petar Todorovic¹, Fengwang Li¹, Tao-Tao Zhuang¹, Christine M. Gabardo^{1,2}, Ahmad R. Kirmani⁷, Christopher McCallum², Sung-Fu Hung¹, Yanwei Lum¹, Mingchuan Luo¹, Yimeng Min¹, Aoni Xu¹, Colin P. O'Brien², Bello Stephen⁸, Bin Sun¹, Alexander H. Ip¹, Lee J. Richter⁷, Shana O. Kelley^{4,9}, David Sinton^{1,2} and Edward H. Sargent¹✉

The carbon dioxide electroreduction reaction (CO₂RR) provides ways to produce ethanol but its Faradaic efficiency could be further improved, especially in CO₂RR studies reported at a total current density exceeding 10 mA cm⁻². Here we report a class of catalysts that achieve an ethanol Faradaic efficiency of (52 ± 1)% and an ethanol cathodic energy efficiency of 31%. We exploit the fact that suppression of the deoxygenation of the intermediate HOCCH* to ethylene promotes ethanol production, and hence that confinement using capping layers having strong electron-donating ability on active catalysts promotes C-C coupling and increases the reaction energy of HOCCH* deoxygenation. Thus, we have developed an electrocatalyst with confined reaction volume by coating Cu catalysts with nitrogen-doped carbon. Spectroscopy suggests that the strong electron-donating ability and confinement of the nitrogen-doped carbon layers leads to the observed pronounced selectivity towards ethanol.

Electroreduction of CO₂ to valuable chemicals provides a promising avenue towards the storage of renewable electricity¹. Although a wide range of different products from C₁ to C₃ have been produced^{2–7}, only carbon monoxide (CO), formate and ethylene have been reported with high Faradaic efficiency (FE) at commercially relevant current densities (exceeding 100 mA cm⁻²)^{5–7}. Ethanol is of particular interest as it has high energy density and is used as a high-octane fuel. It has a correspondingly high market price and consistent global demand⁸. Today the global market size for ethanol is valued at US\$75 billion a year⁹. In CO₂RR, ethanol and ethylene are the two main competing C₂ products. It is believed that they are derived from a shared key intermediate (HOCCH*), and that ethylene is generated after C–O bond-breaking from HOCCH*^{10,11}. A techno-economic analysis of CO₂RR systems shows that C₂ production can become profitable only once the partial current density exceeds 100 mA cm⁻² (ref. 8). Recently, CO₂RR to ethylene has been reported with an FE of up to 70% with a partial current density of 184 mA cm⁻² (ref. 6). Unfortunately, the best ethanol FE reported so far is 41% even for moderate productivity, that is, having a total current density higher than 10 mA cm⁻² (Supplementary Table 1)^{4,12–16}.

Confinement—covering an active electrocatalyst to enable molecules and solutions to intercalate—is a strategy to modulate the activity of catalysts^{17–19}: confined sub-nanometre-thick spaces

function as nanoreactors. The strategy has been used in the conversion of CO, syngas and methane and in the electrolysis of water^{18,20}. Here we exploit confinement to increase selectivity for ethanol. Density functional theory (DFT) calculations suggest that coating a nitrogen-doped carbon (N-C) layer on a Cu surface promotes C–C coupling and suppresses the breaking of the C–O bond in HOCCH*, thereby promoting ethanol selectivity in CO₂RR. This is made possible by the strong electron-donating ability of the confining N-C layer. The catalyst delivers an ethanol FE of (52 ± 1) % and an ethanol cathodic energy efficiency (EE) of 31%.

DFT calculations

We investigated the CO dimerization reaction (Fig. 1a, Supplementary Figs. 1–4, and Supplementary Table 2), a key step for C₂₊ production, on three structures: a N-C layer on the Cu surface (N-C/Cu); a carbon layer on the Cu surface (C/Cu); and Cu. N-C/Cu has the lowest barrier and enthalpy change for CO dimerization compared to C/Cu and Cu (Fig. 1b), suggesting that N-C/Cu will deliver the highest selectivity to C₂₊ products. In contrast, C/Cu has worse CO dimerization kinetics compared to bare Cu, indicating that the carbon cover on Cu will work against C-C coupling for C₂₊ products.

To understand how the N-C layer affects CO dimerization, we also generated electron density difference plots for N-C/Cu and

¹Department of Electrical and Computer Engineering, University of Toronto, Toronto, Ontario, Canada. ²Department of Mechanical and Industrial Engineering, University of Toronto, Toronto, Ontario, Canada. ³Advanced Light Source, Lawrence Berkeley National Laboratory, Berkeley, CA, USA.

⁴Center for Nanophase Materials Sciences, Oak Ridge National Laboratory, Oak Ridge, TN, USA. ⁵Department of Materials Science and Engineering, University of Toronto, Toronto, Ontario, Canada. ⁶Department of Chemistry, University of Toronto, Toronto, Ontario, Canada. ⁷Materials Science and Engineering Division, National Institute of Standards and Technology (NIST), Gaithersburg, MD, USA. ⁸Hitachi HTA Microscopy Lab, Hillsboro, OR, USA.

⁹Department of Pharmaceutical Sciences, Leslie Dan Faculty of Pharmacy, University of Toronto, Toronto, Ontario, Canada. ¹⁰These authors contributed equally: Xue Wang, Ziyun Wang. ✉e-mail: ted.sargent@utoronto.ca

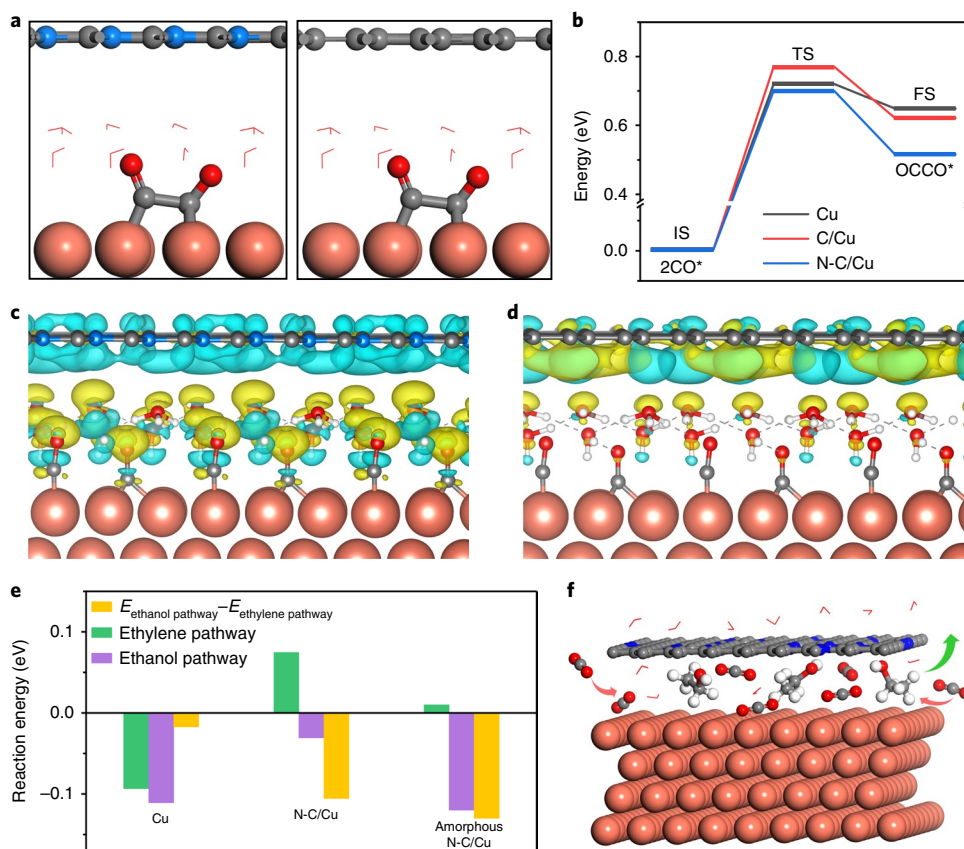


Fig. 1 | DFT calculations. Cu, N, C and O atoms are illustrated as orange, blue, grey and red balls, respectively, while water molecules are shown as lines. **a**, Geometries of dimerized OCCO* intermediate on N-C/Cu and C/Cu. **b**, Energy profiles for initial states (ISs), transition states (TSs), and final states (FSs) of CO dimerization on Cu, C/Cu and N-C/Cu, respectively. **c,d**, Electron density difference plots for N-C/Cu (**c**) and C/Cu (**d**) with two adsorbed *CO and one charged water layer, respectively. Yellow contours represent charge accumulations, and blue contours denote charge depletions. **e**, Reaction energies of the ethylene pathway (HOCCH* to CCH*) and the ethanol pathway (HOCCH* to HOCHCH*) on Cu, N-C/Cu and amorphous N-C/Cu. **f**, Illustration of CO₂ intercalation at the N-C/Cu interface and the production of ethanol.

C/Cu with two adsorbed *CO intermediates in solution (Fig. 1c,d). The N-C layer loses electrons (blue) and the adsorbed *CO gains electrons (yellow), whereas there is no obvious electron transfer between the carbon layer and the adsorbed *CO, suggesting that the N-C layer is beneficial to electron transfer to adsorbed *CO on Cu, and that it thus promotes the generation of the C–C coupled intermediate²¹.

HOCCH* is the key intermediate from which branches the ethylene pathway and the ethanol pathway (Supplementary Fig. 5)^{10,11}; we therefore further calculated the reaction energies of HOCCH* to CCH* (ethylene pathway) and HOCCH* to HOCHCH* (ethanol pathway) to understand the effect of different confining materials on the C₂ product distribution (Supplementary Figs. 6–9 and Supplementary Tables 3–6). Compared to bare Cu, the C/Cu and N-C/Cu catalysts improve ethanol selectivity versus ethylene (Fig. 1e and Supplementary Table 3), which we ascribe to the confinement effect in the stabilization of the C–O bond of HOCCH*, which leads to a suppression of the deoxygenation process. Here the distance between Cu and graphene or a nitrogen-doped graphene layer ($d_{\text{N-C/Cu}}$) was optimized with the aid of DFT (Supplementary Table 7 and Supplementary Figs. 10–12), and the results showed that ethanol selectivity can be promoted in N-C/Cu with $d_{\text{N-C/Cu}}$ in the range 6–9 Å compared to Cu alone. Additionally, we calculated the reaction energies of the ethanol and ethylene pathways based on amorphous N-doped carbon/Cu (amorphous N-C/Cu) (Supplementary Figs. 13–15 and Supplementary Tables 8 and 9). Amorphous N-C/Cu

also improves ethanol selectivity versus ethylene compared to bare Cu (Fig. 1e). Interestingly, the ethanol pathway on both N-C/Cu and amorphous N-C/Cu is favoured thermodynamically, whereas the ethylene pathway is suppressed, suggesting that C–O bond-breaking from HOCCH* is prevented on both N-C/Cu and amorphous N-C/Cu. These results suggest that N-C/Cu has the potential to generate an increased selectivity to ethanol (Fig. 1f).

Catalyst synthesis and characterization

We sought to fabricate N-C/Cu catalysts via sputter deposition of a layer of Cu nanoparticles on the surface of polytetrafluoroethylene (PTFE) nanofibres (Supplementary Figs. 16–18), followed by the sputter deposition of a layer of N-C on the surface of sputtered Cu nanoparticles (Fig. 2a and Supplementary Figs. 17–20). Energy-dispersive X-ray spectroscopy (EDX) elemental mapping shows a uniform distribution of Cu, N and C on PTFE nanofibres (Fig. 2b). Electron microscopy investigations confirm that the N-C layer coated the Cu (Fig. 2c–e and Supplementary Fig. 21). Powder X-ray diffraction (XRD) and transmission wide-angle X-ray scattering (WAXS) data for this electrode demonstrate the presence of Cu; there is no observable peak or ring for the N-C layer, indicating its amorphous structure (Supplementary Figs. 22–24). The N-C layer was confirmed by high-resolution X-ray photoelectron spectroscopy (XPS) C 1s and N 1s spectra (Fig. 2f, g). The deconvoluted C 1s peak shows graphitic carbon and the existence of nitrogen atoms²². The deconvoluted N 1s peak shows that the primary

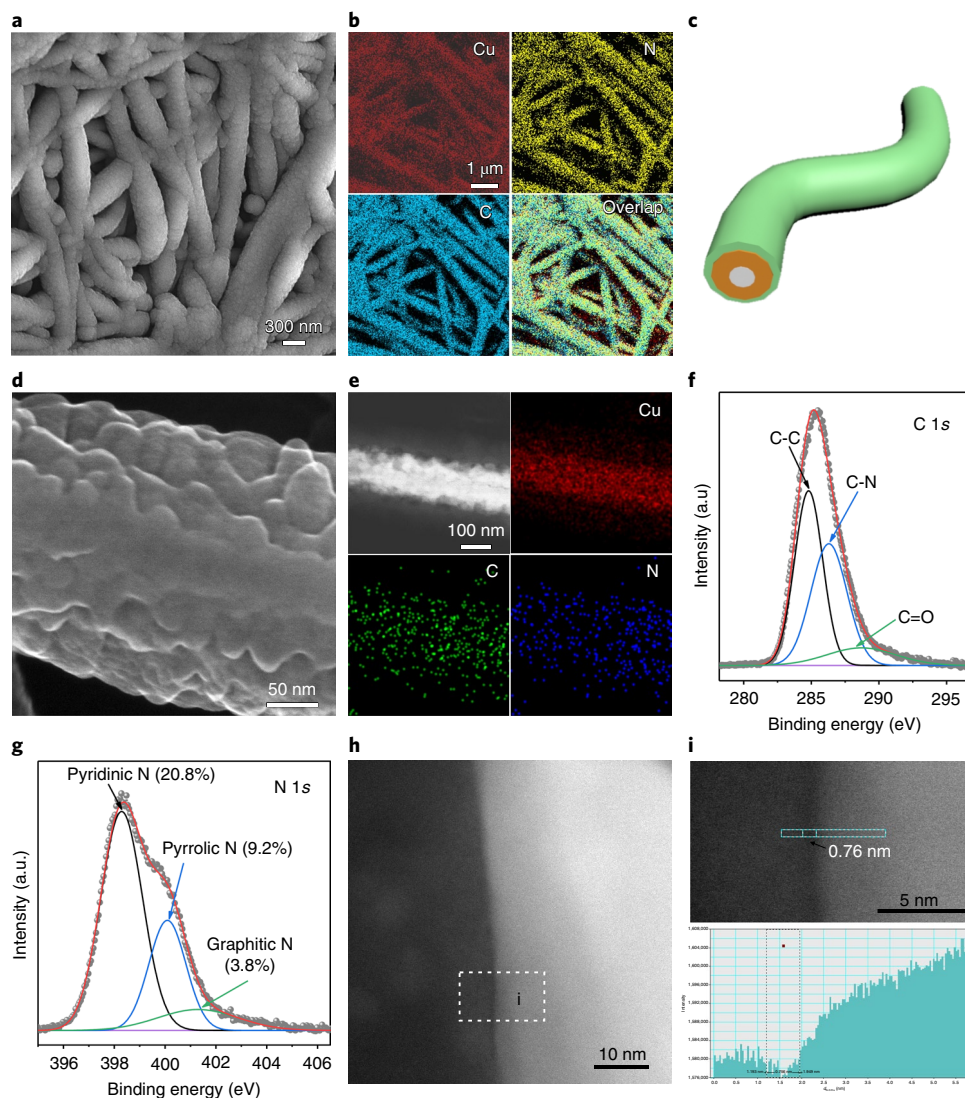


Fig. 2 | Structural and compositional analyses of the 34% N-C/Cu catalyst on PTFE. **a**, Low-magnification scanning electron microscopy (SEM) image of the 34% N-C/Cu catalyst on PTFE. **b**, EDX elemental mapping of Cu, N and C for the 34% N-C/Cu catalyst on PTFE. **c**, Scheme of the cross-sectional structure of a N-C/Cu/PTFE nanofibre. The white, orange and green layers represent PTFE, Cu and N-C, respectively. **d**, **e**, Secondary electron image (**d**) and the corresponding high-angle annular dark-field scanning transmission electron microscopy (HAADF-STEM) image, as well as the elemental mapping of Cu, N and C taken from a section of one 34% N-C/Cu/PTFE nanofibre (**e**). **f**, **g**, High-resolution C 1s (**f**) and N 1s (**g**) spectra for 34% N-C/Cu catalyst on PTFE. (a.u., arbitrary units.) **h**, HAADF-STEM image of the 34% N-C/Cu ultrathin section. **i**, Higher-magnification HAADF-STEM image (top) taken from the area marked by the box in **h** and its intensity profile (the unit of intensity is a.u.) taken along the rectangular frame (bottom), displaying the distance between the Cu layer and the N-C layer, $d_{\text{N-C/Cu}}$.

form of N is pyridinic-N¹⁴ and the atomic percentage of nitrogen in the N-C layer is approximately 34%, as determined by XPS (denoted 34% N-C).

Analysis of HAADF-STEM images of microtomed 34% N-C/Cu catalyst demonstrates that there are regions in which a gap is present between the Cu layer and the N-C layer; and there exist other regions in which these layers touch one another (Fig. 2h and Supplementary Fig. 25a). These images are acquired with a convergence angle of 30 mrad and with an inner collection angle of 65 mrad of a HAADF detector. The HAADF image intensity is approximately proportional to the atomic number $Z^{1.7}$ of the elements²³ and these images can thus be used to differentiate between the Cu and N-C layers. The reduced contrast between the Cu and N-C layers indicates the presence of a gap between these layers; and the intensity profile of this reduced-contrast region can thus be used to estimate the gap

width. In the gap regions, the distance between the Cu layers and the N-C layer that we determined is typically less than 1 nm (Fig. 2i and Supplementary Fig. 25b). We point out that this structural analysis of an ultrathin slice provides overall guidance, but that the absolute value of the gap width cannot be confidently obtained using this method. We reason nevertheless that, for the range of gap widths estimated, the gap regions are able to act as nanoreactors.

Investigation of CO₂ electroreduction

The N-C/Cu electrode was electrochemically tested (Supplementary Fig. 26) in a flow cell reactor, a configuration similar to that used in a previous report²⁴. Figure 3a shows the FE values for C₂₊ products on the 34% N-C/Cu catalyst in the current density range 100–300 mA cm⁻² in 1 M KOH electrolyte. Both FE values of C₂₊ products and ethanol on the 34% N-C/Cu catalyst are

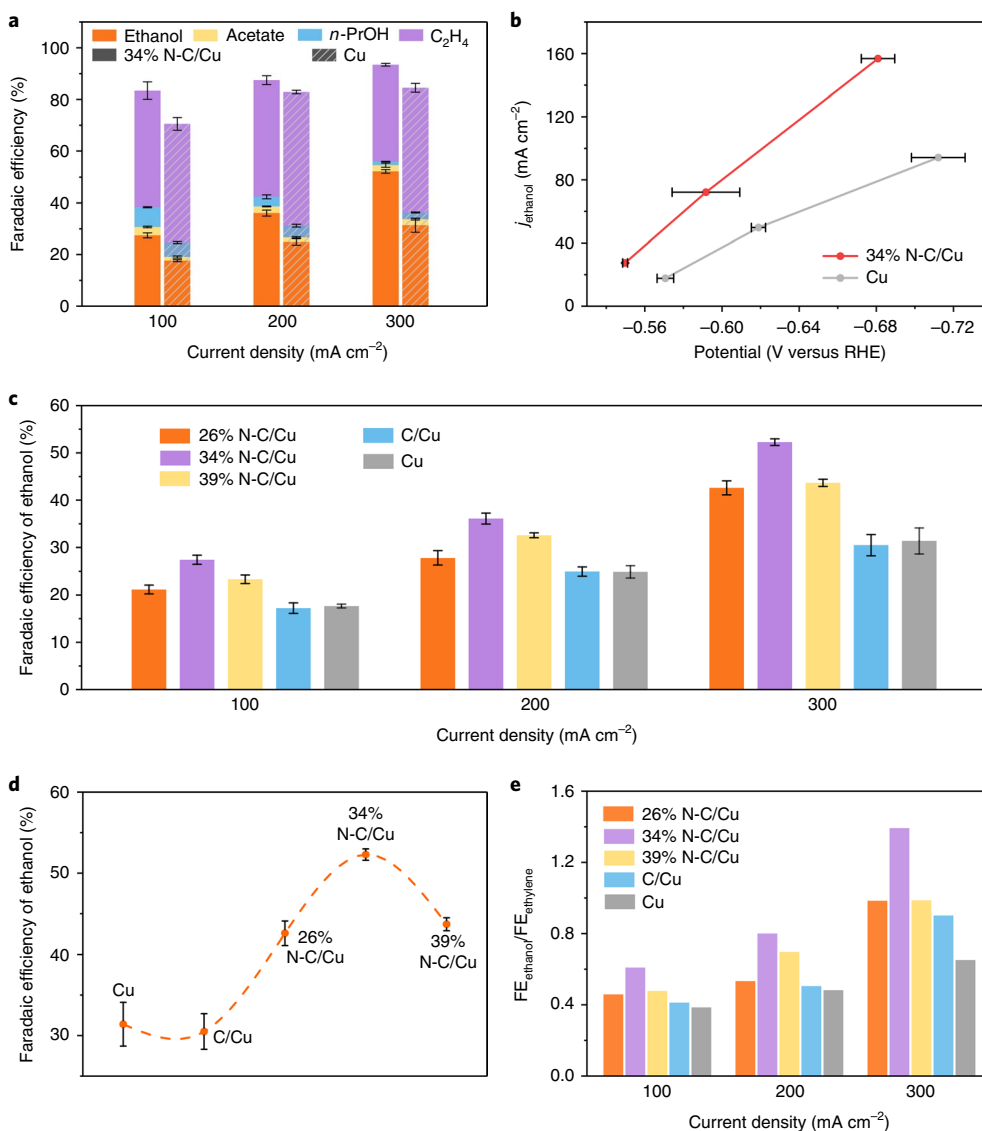


Fig. 3 | CO₂RR performance comparisons. **a**, FE values of C₂₊ products on Cu (the hatched bars) and 34% N-C/Cu catalysts under different current densities. Error bars represent the standard deviation of measurements based on three independent samples. **b**, Partial ethanol current densities j_{ethanol} versus potentials referred to the reversible hydrogen electrode (RHE) on 34% N-C/Cu and Cu catalysts. Error bars denote the standard deviation of potentials ($n > 300$) during the constant-current electrolysis. **c**, Ethanol FE values on different catalysts under different current densities. Error bars represent the standard deviation of measurements based on three independent samples. **d**, Comparison of ethanol FE values for different catalysts at 300 mA cm⁻². Error bars represent the standard deviation of measurements based on three independent samples. **e**, Comparison of the ratios of FE_{ethanol} to FE_{ethylene} on different catalysts under different current densities.

higher than that on the bare Cu control (Supplementary Table 10), in agreement with our DFT prediction. Under a current density of 300 mA cm⁻², the total C₂₊ FE on 34% N-C/Cu is up to 93% and an ethanol FE of (52 ± 1)% is achieved with a conversion rate of (156 ± 3) mA cm⁻² at -0.68 V with reference to the reversible hydrogen electrode (V_{RHE}) after ohmic loss correction (Fig. 3b and Supplementary Fig. 27); this represents an ethanol cathodic EE of 31%. In addition, we note that the H₂ FE on 34% N-C/Cu is lower than that on bare Cu (Supplementary Table 10), also in agreement with DFT calculations (Supplementary Table 11). We also evaluated the CO₂RR performance on a bare 34% N-C layer; only H₂ with FE up to 80–90% could be detected (Supplementary Fig. 28): there was no ethanol detectable in the electrolyte following CO₂RR, indicating that the ultrathin N-C layer does not, on its own, catalyse CO₂RR to ethanol.

We estimated the electrochemically active surface area of Cu (Cu_{ECSA}) in N-C/Cu and Cu catalysts using Pb underpotential deposition (Pb_{UPD}) (Supplementary Fig. 29 and Supplementary Table 12). We normalized the partial ethanol current density by Cu_{ECSA} to compare intrinsic activity (Supplementary Fig. 30) and found that, under optimal ethanol conditions (300 mA cm⁻²), the Cu_{ECSA} -normalized partial ethanol current density on 34% N-C/Cu is 26.6 mA cm⁻², which is 1.8 times higher than that on Cu. We further performed isotope-labelling experiments with ¹³CO₂ and found that ethanol was indeed produced via CO₂RR, rather than from contaminants (Supplementary Figs. 31 and 32).

To explore the effects of the N-C layer on the performance of CO₂RR, we also prepared 26% N-C/Cu, 39% N-C/Cu and C/Cu on PTFE via similar sputtering methods (Supplementary Figs. 33–36) and measured their CO₂RR performance for comparison (Fig. 3c–e).

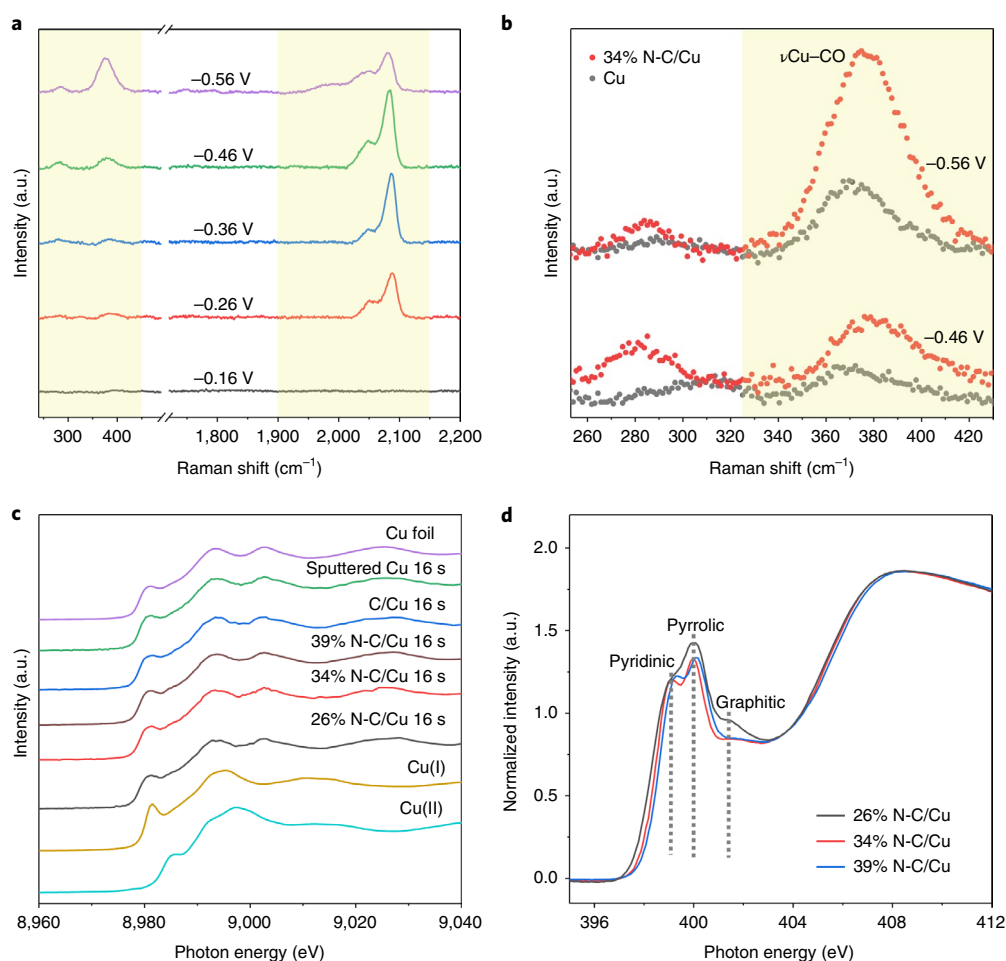


Fig. 4 | In situ Raman and XAS characterization. **a**, In situ Raman spectra of the 34% N-C/Cu catalyst during CO₂RR under different applied potentials. The regions of 240–450 cm⁻¹ and 1,900–2,150 cm⁻¹ are shaded. **b**, Comparison of in situ Raman spectra of 34% N-C/Cu and Cu catalysts in the range of 253–430 cm⁻¹. The region of 325–430 cm⁻¹ showing Cu–CO stretch (ν Cu–CO) is shaded. All given potentials are referred to the reversible hydrogen electrode (RHE). **c**, In operando Cu K-edge XANES spectra of different catalysts during CO₂RR by applying 300 mA cm⁻² for 16 s. Bulk Cu foil, CuO and Cu₂O are listed as references. **d**, Surface-sensitive total-electron-yield XANES spectra at the nitrogen K-edge on different N-C/Cu catalysts.

Under the same current densities, 26% N-C/Cu and 39% N-C/Cu catalysts also deliver a higher C₂₊ FE than Cu catalysts, whereas the C/Cu catalyst shows a lower C₂₊ FE compared to the Cu catalyst (Supplementary Table 10), suggesting that the confinement of the carbon layer on Cu could not favour C–C coupling for C₂₊ products. All the N-C/Cu catalysts showed higher selectivities to ethanol relative to the Cu and C/Cu catalysts under the same current densities (Fig. 3c). By comparing the CO₂RR performance at 300 mA cm⁻² among the catalysts, the 34% N-C/Cu catalyst displays the highest ethanol FE, 1.7× higher than for the Cu control (Fig. 3d). We further calculated the ratios of ethanol FE to ethylene FE (FE_{ethanol}/FE_{ethylene}) to evaluate the selectivity to ethanol versus ethylene in CO₂RR (Fig. 3e). Compared with Cu, all the N-C/Cu and C/Cu catalysts exhibit higher FE_{ethanol}/FE_{ethylene}, in agreement with our calculations, indicating that the confinement of the cover on Cu is more favourable for the ethanol pathway versus the ethylene pathway.

To compare local pH at the Cu surface in N-C/Cu and Cu, we carried out the local species concentration modelling for cases with and without the N-C layer (Supplementary Fig. 37). The local pH at the Cu surface is unchanged (Supplementary Table 13).

It is well known that the formation of multi-carbon products in CO₂RR goes through the formation of the *CO intermediate, and then the further reduction of *CO intermediates^{11,25,26}. To gain insight into C–C coupling on 34% N-C/Cu and Cu electrodes

during CO₂RR, we acquired Raman spectra in situ and investigated the interactions between the catalytic surface and the *CO intermediate (Fig. 4a,b). Three regions in Raman spectra are associated with the surface-absorbed *CO. The bands at about 283 cm⁻¹ and about 374 cm⁻¹ are related to the Cu–CO frustrated rotation and Cu–CO stretch, respectively^{27,28}. The band in the range 1,900–2,120 cm⁻¹ can be ascribed to the C≡O stretch of the surface-absorbed CO, including atop-bound CO (>2,000 cm⁻¹) and bridge-bound CO (1,900–2,000 cm⁻¹) (ref. 29,30). Raman spectra with Ar-saturated KOH were also measured as controls to reveal that it was truly CO₂-saturated conditions that gave rise to these multiple sets of peaks (Supplementary Fig. 38). In situ Raman spectra shows that the peaks related to the surface-absorbed *CO appear at a more positive potential on 34% N-C/Cu catalyst (–0.26 V_{RHE}) relative to the bare Cu catalyst (–0.46 V_{RHE}) (Supplementary Fig. 39), indicating that the potential for CO generation on the 34% N-C/Cu is lower than that on Cu.

We also found that, under the same potentials, the bands for the Cu–CO stretch exhibited a blueshift on the 34% N-C/Cu compared to Cu (Fig. 4b). The blueshift suggests a stronger binding of CO to the N-C/Cu surface relative to Cu (ref. 31), which might promote the subsequent C–C coupling step and thus the production of C₂₊ (ref. 32). We also calculated the CO adsorption energies on the N-C/Cu and Cu models using DFT and found that the CO adsorption energy on

the N-C/Cu (-0.60 eV) was also higher than that on Cu (-0.48 eV) (Supplementary Table 14), consistent with our Raman results.

We also performed in operando X-ray absorption spectroscopy (XAS) at the Cu K-edge to investigate the Cu chemical state during CO₂RR. Under the current density of 300 mA cm^{-2} , all copper oxides in the different N-C/Cu and Cu catalysts are reduced to Cu(0) within the first 16 s, and then the valence state of Cu is maintained at zero throughout CO₂RR (Fig. 4c and Supplementary Figs. 40 and 41). These in operando XAS results demonstrate that the selectivity to ethanol on the N-C/Cu and Cu catalysts is associated with the metallic state of Cu, rather than the existence of copper oxides^{11,33}. Additionally, there is no feature of Cu-C or Cu-N in the in operando XAS results³⁴, suggesting that no chemical bond is formed between the Cu layer and the N-C (or C) layer and thus the interaction between the Cu layer and the N-C (or C) layer is of the van der Waals type. This is sufficient to render the N-C/Cu and C/Cu catalysts stable during the CO₂RR reaction. Ex situ XAS at the potassium K-edge on the 34% N-C/Cu catalyst following CO₂RR reveals the adsorption of K⁺ on Cu (Supplementary Fig. 42), suggesting a non-continuous interface between the Cu and N-C layers—supporting the results of the HAADF-STEM images (Fig. 2h and Supplementary Fig. 25).

We note that ethanol FE shows a volcano-shape relationship with the increase of nitrogen contents under the same current densities (Fig. 3d and Supplementary Fig. 43). This trend might be related to the different electron-donating abilities of N-C layers on Cu catalysts. In the N-C layer, pyridinic-N is the main factor determining the electron-donating ability as it has a lone electron pair in the plane of the carbon matrix³⁵. Among the N-C/Cu catalysts, the highest content of pyridinic-N in 34% N-C/Cu may thus lead to the highest ethanol FE (Fig. 2f and Supplementary Fig. 36).

Additionally, we also acquired ex situ X-ray absorption near-edge structure (XANES) spectra at the nitrogen K-edge on different N-C/Cu catalysts in total-electron-yield mode, which provided information on the near-surface chemical states³⁶ (Fig. 4d). Nitrogen K-edge XANES spectra also show that there are three types of nitrogen doping (pyridinic-N, pyrrolic-N and graphitic-N) in the N-C/Cu catalysts³⁷. As the concentration of doped nitrogen increases in the N-C layer, the main adsorption edges shift to higher energy, demonstrating that the average valence state of the nitrogen atoms (negative charge) increases in the order of 26% N-C < 34% N-C/Cu < 39% N-C/Cu. The nitrogen K-edge XANES spectra of different N-C/Cu catalysts recorded in a bulk-sensitive partial fluorescence yield³⁶ also show the same trend (Supplementary Fig. 44). Among these N-C/Cu catalysts, a nitrogen atom with a lower valence state has a stronger electron-donating ability, and thus favours electron transfer from the N-C layers to the surface intermediates and ultimately promotes ethanol production during CO₂RR, as discussed for the DFT calculations. Apart from the average valence state of the nitrogen atoms, the total electron-donating ability of the N-C layer is also determined by the proportion of doped nitrogen. Therefore, the moderate valence state of the nitrogen atoms and the concentration of nitrogen in the 34% N-C/Cu catalyst might result in the strongest total electron-donating ability, thereby delivering the highest ethanol FE.

We integrated the 34% N-C/Cu catalyst into a membrane electrode assembly (MEA) system to evaluate its stability (Supplementary Fig. 45). This system shows an ethanol FE value similar to that of the alkali flow cell, and also retains the high ratio of FE_{ethanol} to FE_{ethylene} seen in the alkali system (Supplementary Figs. 46 and 47). After we had operated the MEA system under a full-cell voltage of -3.67 V for 15 h with a total current density of about 160 mA cm^{-2} , the system retained its ethanol FE of 52%, representing an ethanol full-cell EE of 16% (Supplementary Fig. 48). XRD, SEM and EDX elemental mapping show that the N-C/Cu catalyst maintains its structure and morphology following 15 h of high-intensity electrolysis (Supplementary Figs. 49 and 50).

Conclusions

This work reports how the confinement effect, arising from an N-C layer on Cu catalysts, taken together with the strong electron-donating ability of the N-C layer, enables advances in selectivity towards ethanol in CO₂RR. We report an ethanol FE of $(52 \pm 1)\%$ with a partial ethanol current density $(156 \pm 3) \text{ mA cm}^{-2}$ on the 34% N-C/Cu catalyst in CO₂RR. The cathodic EE and full-cell EE values for ethanol are also high, at 31% and 16%, respectively. These findings provide a route towards improving selectivity towards high-energy-density ethanol in CO₂RR through catalyst design.

Methods

Chemicals. Copper target (99.999%) and carbon graphite target (99.999%) were purchased from the Kurt J. Lesker company. (Certain commercial equipment, instruments or materials are identified in this paper and the Supplementary Information in order to specify the experimental procedure adequately. Such identification is not intended to imply recommendation or endorsement by the National Institute of Standards and Technology, nor is it intended to imply that the materials or equipment identified are necessarily the best available for the purpose.) Potassium hydroxide (KOH) was purchased from Caledon Laboratory Chemical. Iridium (III) chloride hydrate ($\text{IrCl}_3 \cdot x\text{H}_2\text{O}$, 99.9%) and potassium bicarbonate (KHCO_3 , 99.5%) were purchased from Sigma-Aldrich. Anion exchange membrane (Fumasep FAB-PK-130), gas diffusion layer (Freudenberg H14C9), and titanium mesh were obtained from Fuel Cell Store. A Sustainion anion-exchange membrane was obtained from Dioxide Materials; the membrane was activated in 1 M KOH aqueous solution for 24 h and then washed with water before use. PTFE membrane with an average pore size of 450 nm was purchased from Beijing Zhongxingweiye Instrument Co., Ltd. Ni foam (1.6 mm thickness) was purchased from MTI Corporation. All chemicals were used as received. All aqueous solutions were prepared using deionized water with a resistivity of $18.2 \text{ M}\Omega \text{ cm}^{-1}$.

Electrodes. All the cathodes were prepared using a magnetron sputtering system. Typically, a Cu cathode was prepared by sputtering 200 nm Cu catalyst (Cu target, sputtering rate about 1.1 \AA s^{-1}) onto a piece of PTFE membrane. The mass loading of Cu on the PTFE membrane is 0.19 mg cm^{-2} . By sputtering 50 nm of the N-C layer or the carbon layer (carbon graphite target, sputtering rate about 0.05 \AA s^{-1}) on sputtered Cu catalysts supported by PTFE, we can further obtain the N-C/Cu and C/Cu cathodes, respectively. N-C layers with different nitrogen contents were prepared by adjusting the flow rate ratio of N₂ to Ar. For deposition of carbon, 26%, 34% and 39% N-C layers on sputtered Cu catalysts, the flow rate ratios of N₂ to Ar were set to be 0/20 standard cubic centimetres per minute (sccm), 2/20 sccm, 6/20 sccm and 20/20 sccm, respectively. Similarly, the 34% N-C gas diffusion electrode was prepared by sputtering 50 nm of the N-C layer onto the gas diffusion layer.

In the flow cell, Ag/AgCl reference electrode (3 M KCl, BASi) and Ni foam were used as the reference electrode and anode, respectively. In the MEA system, the iridium oxide supported on titanium mesh (IrOx/Ti mesh) used as the anode catalyst was prepared using a dip-coating and thermal-decomposition method³⁸.

Structural and compositional analyses. SEM images and the corresponding EDX elemental mapping were taken using a Hitachi FE-SEM SU5000 microscope. HAADF-STEM images, and the corresponding EDX and electron energy loss spectroscopy (EELS) elemental mapping were taken using a Hitachi HF-3300 microscope at 300 kV and an aberration-corrected FEI Titan 80–300 kV transmission electron microscopy (TEM)/STEM microscope at 300 kV, with a probe convergence angle of 30 mrad and a large inner collection angle of 65 mrad to provide a nominal image solution of 0.7 Å. For the TEM/STEM imaging, we prepared an ultrathin slice (about 100 nm) using the Leica UM7 ultramicrotome (Leica Microsystems). The slice was then transferred to a 100-mesh nickel grid for characterization. Cross-sectional SEM imaging and EDX elemental mapping were performed using a Hitachi Dual-beam FIB-SEM NB5000. Structural characterization of cathodes was obtained using XRD (MiniFlex600) with Cu K α radiation. The surface compositions of cathodes were determined by XPS (model 5600, Perkin-Elmer) using a monochromatic aluminum X-ray source. In situ Raman measurements were obtained using a Renishaw inVia Raman microscope in a modified flow cell and a water immersion objective (63 \times) with a 785-nm laser. XAS measurements were conducted at the 9BM beamline at the Advanced Photon Source (Argonne National Laboratory). Ex situ XAS measurements were carried out at the BL731 beamline at the Advanced Light Source (Lawrence Berkeley National Laboratory) and the SXRMB beamline at the Canadian Light Source. Athena and Artemis software included in a standard IFEFFIT package were used to process the XAS data³⁹. WAXS measurements were carried out in transmission geometry at the CMS beamline of the National Synchrotron Light Source II, a United States Department of Energy (US DOE) office of the Science User Facility operated for the DOE Office of Science by Brookhaven National Laboratory. Samples were measured with an imaging detector at a distance of 0.177 m using an X-ray wavelength of 0.729 Å. The Nika software package was used to sector average

the two-dimensional WAXS images⁴⁰. Data plotting was done using Igor Pro (Wavemetrics; <https://www.wavemetrics.com/products/igorpro>).

Electrochemical measurements. In the flow cell, the electrochemical measurements were conducted in the three-electrode system at an electrochemical station (AUT50783). Prepared cathodes, the anion exchange membrane and nickel foam were positioned and clamped together via PTFE gaskets. Here nickel foam was used as the anode for the oxygen evolution reaction in the flow cell because nickel is a good oxygen-evolution-reaction catalyst in an alkaline environment⁴¹. 30 ml of electrolyte (1 M KOH aqueous solution) was introduced into the anode chamber between the anode and the membrane, as well as the cathode chamber between the membrane and the cathode, respectively. The electrolytes in the cathode and anode were circulated by two pumps at the rate of 10 ml min⁻¹. Meanwhile, CO₂ gas (Linde, 99.99%) was continuously supplied to the gas chamber located at the back side of the cathode at the rate of 50 ml min⁻¹. Through the pore of the cathode, gas could diffuse into the interface between the cathode and the electrolyte. The performance of the cathodes was evaluated by performing constant-current electrolysis. All potentials were measured against an Ag/AgCl reference electrode (3 M KCl, BASi). In the isotope-labelling experiment, the procedure was the same as in the above experiment, except that ¹³CO₂ gas (Sigma-Aldrich, 99 atom% ¹³C) was used as the supply gas.

Gas and liquid products were analysed using a gas chromatograph (PerkinElmer Clarus 600) equipped with thermal conductivity and flame ionization detectors and a nuclear magnetic resonance (NMR) spectrometer (Agilent DD2 600 MHz) by taking dimethylsulfoxide (DMSO) as an internal standard, respectively. All the potentials were converted to values with reference to the RHE using:

$$E_{\text{RHE}} = E_{\text{Ag/AgCl}} + 0.210 \text{ V} + 0.0591 \times \text{pH}$$

The ohmic loss between the working and reference electrodes was measured using the electrochemical impedance spectroscopy technique at the beginning of the electrolysis and 95% *iR* compensation (*i*, current; *R*, uncompensated resistance) was applied to correct the potentials manually.

Cu_{ECSA} in catalysts was determined using Pd underpotential deposition in the flow cell. An N₂-saturated solution of 100 mM HClO₄ + 1 mM Pd(ClO₄)₂ was used as the electrolyte. The cathode was held at -0.081 V_{RHE} for 60 s and then cyclic voltammetry was recorded between -0.281 and 0.239 V_{RHE} at 5 mV s⁻¹. Pt foil was used as the anode. N₂ (Linde, 99.998%) was continuously supplied to the gas chamber of the flow cell. The electrolyte was not circulated during the cyclic voltammetry measurement. The Cu_{ECSA} in the catalyst is calculated from the charge associated with 2e⁻ oxidation of monolayer of Pd adatoms coverage over Cu surface with a conversion factor of 310 μC cm⁻² (ref. 42).

The MEA was a complete 5 cm² CO₂ electrolyser (SKU 68732), purchased from Dioxide Materials. The cathode catalyst (2.25 cm by 2.25 cm) was attached on the cathode side by the copper tape at the edge of the electrode and Kapton tape was then attached on the top of copper tape to avoid its contact with the membrane/electrolyte. The activated Sustainion membrane (3 cm × 3 cm) and five pieces of IrO₂/Ti mesh anode catalyst (2.25 cm by 2.25 cm) were placed on the top of the cathode successively and then assembled together in MEA, as shown in Supplementary Fig. 45. On the anode side, 0.2 M KHCO₃ aqueous solution was used as the anolyte and was circulated using a pump at the rate of 10 ml min⁻¹. On the cathode side, CO₂ gas (80 ml min⁻¹) continuously flowed to the humidifier with deionized water and was then supplied to the cathode chamber of MEA. The performance of the catalysts in the MEA system was evaluated by applying different full-cell potentials in the two-electrode system at the electrochemical station (AUT50783) equipped with a current boost (10 A). The gas products were collected and tested by gas chromatograph after the products from the cathode side went through a simplified cold trap (Supplementary Fig. 45). Owing to the liquid product crossover, the FE values of the liquid products were calculated based on the total amount of the products collected on the anode and cathode sides during the same period.

Calculation for energy conversion efficiency. In the flow cell, the ethanol energy conversion efficiency was calculated for the half-cell in the cathode (EE_{cathodic half-cell}). The overpotential of oxygen evolution is assumed to be zero. The ethanol EE_{cathodic half-cell} can be calculated as follows⁴³:

$$EE_{\text{cathodic half-cell}} = \frac{(1.23 + (-E_{\text{ethanol}})) \times FE_{\text{ethanol}}}{(1.23 + (-E_{\text{applied}}))}$$

where *E*_{applied} is the potential used in the experiment, FE_{ethanol} is the measured Faradaic efficiency of ethanol in percentage, and *E*_{ethanol} = 0.09 V_{RHE} for CO₂RR (ref. 43).

In MEA system, ethanol energy efficiency is calculated for full cell:

$$EE_{\text{full-cell}} = \frac{(1.23 + (-E_{\text{ethanol}})) \times FE_{\text{ethanol}}}{-E_{\text{full-cell applied}}}$$

where *E*_{full-cell applied} is the full-cell voltage applied in the MEA system.

Theoretical methods. In this work, all the DFT calculations were carried out with a periodic slab model using the Vienna ab initio simulation program (VASP)^{44–47}. The generalized gradient approximation was used with the Perdew–Burke–Ernzerhof exchange–correlation functional⁴⁸. The projector-augmented wave method^{49,50} was utilized to describe the electron–ion interactions, and the cut-off energy for the plane-wave basis set was 450 eV. To illustrate the long-range dispersion interactions between the adsorbates and catalysts, we employed the D3 correction method by Grimme et al.⁵¹ Brillouin zone integration was accomplished using a 3×3×1 Monkhorst–Pack *k*-point mesh.

For the modelling of copper, the crystal structure was optimized, and the equilibrium lattice constants were found to be α_{Cu} = 3.631 Å. We used a 4-layer model with p(3×3) supercell with the two upper layers relaxed and the two lower layers fixed. All the adsorption geometries were optimized using a force-based conjugate gradient algorithm, while transition states were located with a constrained minimization technique^{52–54}. At all intermediate and transition states, one charged layer of water molecules was added to the surface to take the combined effects of field and solvation into account: six water molecules are added near the surface, with three facing toward the surface, and three parallel with the surface⁵⁵. To consider the effect from the confinement of carbon and nitrogen-doped carbon on Cu, we added one layer of graphene or nitrogen-doped graphene on the Cu surface, as shown in Supplementary Fig. 1.

We further developed a sampling framework based on the amorphous study by Deringer et al. (ref. 56). A total of 50 amorphous carbon and 100 amorphous N-doped carbon structures were investigated using the pipeline (Supplementary Fig. 13).

We started the pipeline with the structure of the Cu surface with intermediate and water (defined as structure 1). We then added amorphous carbon structures on the surface of structure 1 and allowed DFT to fully relax the amorphous structures and water molecules. All fifteen amorphous structures were considered from the amorphous study (in folder ‘DFT_relaxed_216at’ of the supplementary material) by Deringer et al. (ref. 56). The formation energy per atom distribution of the optimized amorphous carbon is shown in Supplementary Fig. 14. We checked the energy distribution of the amorphous carbon structures and removed reconstructed structures, such as structures with protons transferred from water to amorphous carbon.

We then kept the top ten most stable unreconstructed amorphous carbon structures, and for each amorphous carbon structure, we randomly replaced 30% carbon with nitrogen ten times. This process generates 100 amorphous N-doped carbon structures, and the formation energy per atom distribution of the 100 structures is shown in Supplementary Fig. 15. We then chose the top ten most stable amorphous N-doped carbon structures (Supplementary Table 7) and calculated the reaction energies of the ethanol and ethylene pathways (Supplementary Table 8). The overall preference of the pathways represents the contribution from all of the structures. The average reaction energies of the ethylene and ethanol pathways are 0.01 eV and -0.12 eV, respectively, indicating that confinement due to amorphous N-doped carbon promotes ethanol selectivity.

Local species concentration modelling. The system was modelled as a two-dimensional domain with 200-nm-thick Cu and 50-nm-thick porous N-C layers, according to the catalyst, as well as electrolyte sub-domains (Supplementary Fig. 34). The local concentrations of CO₂, CO₃²⁻, HCO₃⁻, OH⁻, H⁺ and H₂O in an electrolyte solution under CO₂RR conditions were modelled in COMSOL 5.4 (COMSOL Multiphysics) using the Transport of Dilute Species physics with the values reported in Supplementary Table 9. This model, based on previous papers^{6,57,58}, accounts for the acid–base carbonate equilibria, as well as CO₂ reduction via electrocatalysis in an electrolyte solution (1 M KOH). The quantity of dissolved CO₂ in solution is determined by the temperature, pressure and solution salinity. Assuming CO₂ acts as an ideal gas, the dissolved amount is given by Henry’s law^{59,60}, and the solubility is further diminished owing to the high concentration of ions in solutions according to the Sechenov equation⁶¹. CO₂, CO₃²⁻, HCO₃⁻, OH⁻, H⁺ and H₂O are all in equilibrium in solution according to the acid–base equilibria^{62–65} with flux due to Fickian diffusion⁶⁶, as well as CO₂ reduction and OH⁻ production^{67,68} for a current density of 300 mA cm⁻². A time-dependent study was performed to simulate species evolution towards the steady state. At the perimeter of the outer boundary, the CO₂ concentration was specified according to Henry’s law and the Sechenov effect, with 1 M KOH equilibrium concentrations imposed for CO₃²⁻, HCO₃⁻ and OH⁻. The inner Cu domain is modelled as solid, on the surface of which the CO₂ was reduced and OH⁻ was produced, and the N-C domain is porous—with discrete 10-nm nanopores as well—all of which use Bruggeman effective diffusivity^{69–71}. We set an approximately 1-nm gap between the Cu layer and the N-C layer based on the actual N-C/Cu catalyst. The case for no N-C layer was modelled by excluding the N-C domain with all other parameters kept the same.

Data availability

The authors declare that the data supporting the findings of this study are available within the paper, Supplementary Information and Source Data files.

Received: 25 September 2019; Accepted: 24 March 2020;

Published online: 11 May 2020

References

- Jhong, H.-R., Ma, S. & Kenis, P. J. A. Electrochemical conversion of CO₂ to useful chemicals: current status, remaining challenges, and future opportunities. *Curr. Opin. Chem. Eng.* **2**, 191–199 (2013).
- Hori, Y. Electrochemical CO₂ reduction on metal electrodes. In *Modern Aspects of Electrochemistry* (eds Vayenas, C. G., White, R. E. & Gamboa-Aldeco, M. E.) Vol. 42, Ch. 3 (Springer, 2008).
- Qiao, J., Liu, Y., Hong, F. & Zhang, J. A review of catalysts for the electroreduction of carbon dioxide to produce low-carbon fuels. *Chem. Soc. Rev.* **43**, 631–675 (2014).
- Zhou, Y. et al. Dopant-induced electron localization drives CO₂ reduction to C₂ hydrocarbons. *Nat. Chem.* **19**, 974–980 (2018).
- Ren, R. et al. Molecular electrocatalysts can mediate fast, selective CO₂ reduction in a flow cell. *Science* **365**, 367–369 (2019).
- Dinh, C.-T. et al. CO₂ electroreduction to ethylene via hydroxide-mediated copper catalysis at an abrupt interface. *Science* **360**, 783–787 (2018).
- Xia, C. et al. Continuous production of pure liquid fuel solutions via electrocatalytic CO₂ reduction using solid-electrolyte devices. *Nat. Energy* **4**, 776–785 (2019).
- Jouny, M., Luc, W. & Jiao, F. General techno-economic analysis of CO₂ electrolysis systems. *Ind. Eng. Chem. Res.* **57**, 2165–2177 (2018).
- Global Ethanol Market: Advancement In Production Technologies To Boost Market*, Notes TMR (Transparency Market Research, 2018); www.transparencymarketresearch.com/pressrelease/ethanol-market.htm.
- Lum, Y., Cheng, T., Goddard, W. A. & Ager, J. W. Electrochemical CO reduction builds solvent water into oxygenate products. *J. Am. Chem. Soc.* **140**, 9337–9340 (2018).
- Cheng, T., Xiao, H. & Goddard, W. A. Full atomistic reaction mechanism with kinetics for CO reduction on Cu(100) from ab initio molecular dynamics free-energy calculations at 298 K. *Proc. Natl Acad. Sci. USA* **114**, 1795–1800 (2017).
- Hoang, T. T. H. et al. Nanoporous copper-silver alloys by additive-controlled electrodeposition for the selective electroreduction of CO₂ to ethylene and ethanol. *J. Am. Chem. Soc.* **140**, 5791–5797 (2018).
- Zhuang, T.-T. et al. Steering post-C–C coupling selectivity enables high efficiency electroreduction of carbon dioxide to multi-carbon alcohols. *Nat. Catal.* **1**, 421–428 (2018).
- Wu, J. et al. A metal-free electrocatalyst for carbon dioxide reduction to multi-carbon hydrocarbons and oxygenates. *Nat. Commun.* **7**, 13869 (2016).
- Hoang, T. T. H., Ma, S., Gold, J. I., Kenis, P. J. A. & Gewirth, A. A. Nanoporous copper films by additive-controlled electrodeposition: CO₂ reduction catalysis. *ACS Catal.* **7**, 3313–3321 (2017).
- Li, F. et al. Cooperative CO₂-to-ethanol conversion via enriched intermediates at molecule–metal catalyst interfaces. *Nat. Catal.* **3**, 75–82 (2020).
- Li, H., Xiao, J., Fu, Q. & Bao, X. Confined catalysis under two-dimensional materials. *Proc. Natl Acad. Sci. USA* **114**, 5930–5934 (2017).
- Qiang, F. & Bao, X. Surface chemistry and catalysis confined under two-dimensional materials. *Chem. Soc. Rev.* **46**, 1842–1874 (2017).
- Zicovich-Wilson, C., Corma, A. & Viruela, P. Electronic confinement of molecules in microscopic pores. A new concept which contributes to the explanation of the catalytic activity of zeolites. *J. Phys. Chem.* **98**, 10863–10870 (1994).
- Yang, F., Deng, D., Pan, X., Fu, Q. & Bao, X. Understanding nano effects in catalysis. *Natl Sci. Rev.* **2**, 183–201 (2015).
- Calle-Vallejo, F. & Koper, M. T. M. Theoretical considerations on the electroreduction of CO to C₂ species on Cu(100) electrodes. *Angew. Chem. Int. Ed.* **52**, 7282–7285 (2013).
- Kumar, B. et al. Renewable and metal-free carbon nanofiber catalysts for carbon dioxide reduction. *Nat. Commun.* **4**, 2918 (2013).
- Krivanek, O. L. et al. Atom-by-atom structural and chemical analysis by annular dark-field electron microscopy. *Nature* **464**, 571–574 (2010).
- Zhuang, T.-T. et al. Copper nanocavities confine intermediates for efficient electrosynthesis of C₃ alcohol fuels from carbon monoxide. *Nat. Catal.* **1**, 946–951 (2018).
- Kortlever, R., Shen, J., Schouten, K. J. P., Calle-Vallejo, F. & Koper, M. T. M. Catalysts and reaction pathways for the electrochemical reduction of carbon dioxide. *J. Phys. Chem. Lett.* **6**, 4073–4082 (2015).
- Montoya, J. H., Shi, C., Chan, K. & Nørskov, J. K. Theoretical insights into a CO dimerization mechanism in CO₂. *J. Phys. Chem. Lett.* **6**, 2032–2037 (2015).
- Chernyshova, I., Somasundaran, P. & Ponnurangam, S. On the origin of the elusive first intermediate of CO₂ electroreduction. *Proc. Natl Acad. Sci. USA* **115**, E9261–E9270 (2018).
- Akemann, W. & Otto, A. Vibrational modes of CO adsorbed on disordered copper films. *J. Raman Spectrosc.* **22**, 797–803 (1991).
- Gunathunge, C. M. et al. Spectroscopic observation of reversible surface reconstruction of copper electrodes under CO₂ reduction. *J. Phys. Chem. C* **121**, 12337–12344 (2017).
- Sheppard, N. & Nguyen, T. T. In *Advances in Infrared and Raman Spectroscopy* (eds Clark, R. J. H. & Hester, R. E.) Vol. 5 (Heyden, 1978).
- Fielicke, A., Gruene, P., Meijer, G. & Rayner, D. M. The adsorption of CO on transition metal clusters: a case study of cluster surface chemistry. *Surf. Sci.* **603**, 1427–1433 (2009).
- Sandberg, R. B., Montoya, J. H., Chan, K. & Nørskov, J. K. CO–CO coupling on Cu facets: coverage, strain and field effects. *Surf. Sci.* **654**, 56–62 (2016).
- Li, J. et al. Copper adparticle enabled selective electrosynthesis of *n*-propanol. *Nat. Commun.* **9**, 4614 (2018).
- Huan, T. N. et al. From molecular copper complexes to composite electrocatalytic materials for selective reduction of CO₂ to formic acid. *J. Mater. Chem. A* **3**, 3901–3907 (2015).
- Liu, G., Li, X., Ganesan, P. & Popov, B. N. Development of non-precious metal oxygen-reduction catalysts for PEM fuel cells based on N-doped ordered porous carbon. *Appl. Catal. B* **93**, 156–165 (2009).
- Li, J. et al. Unraveling the origin of visible light capture by core–shell TiO₂ nanotubes. *Chem. Mater.* **28**, 4467–4475 (2016).
- Niwa, H. et al. X-ray absorption analysis of nitrogen contribution to oxygen reduction reaction in carbon alloy cathode catalysts for polymer electrolyte fuel cells. *J. Power Sources* **187**, 93–97 (2009).
- Luc, W., Rosen, J. & Jiao, F. An Ir-based anode for a practical CO₂ electrolyzer. *Catal. Today* **288**, 79–84 (2017).
- Ravel, B. & Newville, M. ATHENA, ARTEMIS, HEPHAESTUS: data analysis for X-ray absorption spectroscopy using IFEFFIT. *J. Synchrotron Radiat.* **12**, 537–541 (2005).
- Jan, I. Nika: software for two-dimensional data reduction. *J. Appl. Crystallogr.* **45**, 324–328 (2012).
- Urbain, F. et al. A prototype reactor for highly selective solar-driven CO₂ reduction to synthesis gas using nanosized Earth-abundant catalysts and silicon photovoltaics. *Energy Environ. Sci.* **10**, 2256–2266 (2017).
- Baturina, O. A. et al. CO₂ electroreduction to hydrocarbons on carbon-supported Cu nanoparticles. *ACS Catal.* **4**, 3682–3695 (2014).
- Kuhl, K. P., Cave, E. R., Abram, D. N. & Jaramillo, T. F. New insights into the electrochemical reduction of carbon dioxide on metallic copper surfaces. *Energy Environ. Sci.* **5**, 7050–7059 (2012).
- Kresse, G. & Furthmüller, J. Efficient iterative schemes for *ab initio* total-energy calculations using a plane-wave basis set. *Phys. Rev. B* **54**, 11169–11186 (1996).
- Kresse, G. & Furthmüller, J. Efficiency of *ab-initio* total energy calculations for metals and semiconductors using a plane-wave basis set. *Comp. Mater. Sci.* **6**, 15–50 (1996).
- Kresse, G. & Hafner, J. *Ab initio* molecular-dynamics simulation of the liquid-metal amorphous-semiconductor transition in germanium. *Phys. Rev. B* **49**, 14251–14269 (1994).
- Kresse, G. & Hafner, J. *Ab initio* molecular dynamics for liquid metals. *Phys. Rev. B* **47**, 558–561 (1993).
- Perdew, J. P., Burke, K. & Ernzerhof, M. Generalized gradient approximation made simple. *Phys. Rev. Lett.* **77**, 3865–3868 (1996).
- Kresse, G. & Joubert, D. From ultrasoft pseudopotentials to the projector augmented-wave method. *Phys. Rev. B* **59**, 1758–1775 (1999).
- Blöchl, P. E. Projector augmented-wave method. *Phys. Rev. B* **50**, 17953–17979 (1994).
- Grimme, S., Antony, J., Ehrlich, S. & Krieg, H. A consistent and accurate *ab initio* parametrization of density functional dispersion correction (DFT-D) for the 94 elements H–Pu. *J. Chem. Phys.* **132**, 154104 (2010).
- Michaelides, A. et al. Identification of general linear relationships between activation energies and enthalpy changes for dissociation reactions at surfaces. *J. Am. Chem. Soc.* **125**, 3704–3705 (2003).
- Liu, Z. P. & Hu, P. General rules for predicting where a catalytic reaction should occur on metal surfaces: a density functional theory study of C–H and C–O bond breaking/making on flat, stepped, and kinked metal surfaces. *J. Am. Chem. Soc.* **125**, 1958–1967 (2003).
- Alavi, A., Hu, P. J., Deutsch, T., Silvestrelli, P. L. & Hutter, J. CO oxidation on Pt(111): an *ab initio* density functional theory study. *Phys. Rev. Lett.* **80**, 3650–3653 (1998).
- Montoya, J. H., Shi, C., Chan, K. & Nørskov, J. K. Theoretical insights into a CO dimerization mechanism in CO₂ electroreduction. *J. Phys. Chem. Lett.* **6**, 2032–2037 (2015).
- Deringer, V. L. et al. Computational surface chemistry of tetrahedral amorphous carbon by combining machine learning and density functional theory. *Chem. Mater.* **30**, 7438–7445 (2018).
- Gupta, N., Gattrell, M. & MacDougall, B. Calculation for the cathode surface concentrations in the electrochemical reduction of CO₂ in KHCO₃ solutions. *J. Appl. Electrochem.* **36**, 161–172 (2006).
- Burdyny, T. et al. Nanomorphology-enhanced gas-evolution intensifies CO₂ reduction electrochemistry. *ACS Sustain. Chem. Eng.* **5**, 4031–4040 (2017).
- Wiesenburg, D. A. & Guinasso, N. L. J. Equilibrium solubilities of methane, carbon monoxide, and hydrogen in water and sea water. *Chem. Eng. Data* **24**, 356–360 (1979).
- Linstrom, P. J. & Mallard, W. G. *NIST Chemistry WebBook* NIST Standard Reference Database Number 69 (NIST, 2018); <https://doi.org/10.18434/T4D303>.

61. Schumpe, A. & Weisenberger, S. Estimation of gas solubilities in salt solutions at temperatures from 273 K to 363 K. *AIChE J.* **42**, 298–300 (1996).
62. Millero, F. J., Graham, T. B., Huang, F., Bustos-Serrano, H. & Pierrot, D. Dissociation constants of carbonic acid in seawater as a function of salinity and temperature. *Mar. Chem.* **100**, 80–94 (2006).
63. Schulz, K. G., Riebesell, U., Rost, B., Thoms, S. & Zeebe, R. E. Determination of the rate constants for the carbon dioxide to bicarbonate inter-conversion in pH-buffered seawater systems. *Mar. Chem.* **100**, 53–65 (2006).
64. Millero, F. J. & Rabindra, N. R. A chemical equilibrium model for the carbonate system in natural waters. *Croat. Chem. Acta* **70**, 1–38 (1997).
65. Mehrbach, C., Culbertson, C. H., Hawley, J. E. & Pytkowicz, R. M. Measurement of the apparent dissociation constants of carbonic acid in seawater at atmospheric pressure. *Limnol. Oceanogr.* **18**, 897–907 (1973).
66. Vanysek, P. *CRC Handbook of Chemistry and Physics* (CRC Press, 1993).
67. Raciti, D., Mao, M. & Wang, C. Mass transport modelling for the electroreduction of CO₂ on Cu nanowires. *Nanotechnology* **29**, 044001 (2017).
68. Sacco, A., Zeng, J., Bejtka, K. & Chiodoni, A. Modeling of gas bubble-induced mass transport in the electrochemical reduction of carbon dioxide on nanostructured electrodes. *J. Catal.* **372**, 39–48 (2019).
69. Newman, J. & Thomas-Alyea, K. E. *Electrochemical Systems* (John Wiley & Sons, 2004).
70. Bernardi, D. M. & Verbrugge, M. W. Mathematical model of a gas diffusion electrode bonded to a polymer electrolyte. *AIChE J.* **37**, 1151–1163 (1991).
71. Das, P. K., Li, X. & Liu, Z.-S. Effective transport coefficients in PEM fuel cell catalyst and gas diffusion layers: beyond Bruggeman approximation. *Appl. Energy* **87**, 2785–2796 (2010).

Acknowledgements

This work was supported by Suncor Energy, the Natural Sciences and Engineering Research Council (NSERC) of Canada, and the CIFAR Bio-Inspired Solar Energy programme. Synchrotron measurements were carried out at the Advanced Photon Source, an Office of Science User Facility operated for the US DOE Office of Science by Argonne National Laboratory, and was supported by the US DOE under contract number DE-AC02-06CH11357, the Canadian Light Source and its funding partners, and the CMS beamline of the National Synchrotron Light Source II, a US DOE Office of the Science User Facility operated for the DOE Office of Science by Brookhaven National Laboratory. This research also used resources of the Advanced Light Source, which is a DOE Office of Science User Facility under contract number DE-AC02-05CH1123, as well as the sources of the Canadian Light Source. The focused ion beam analyses and some of the TEM/STEM and SEM analyses were carried out at the CFI-funded Ontario Centre for the Characterization of Advanced Materials at the University of Toronto. STEM measurements and EELS mapping were performed at the Center for Nanophase Materials Sciences at Oak Ridge National Laboratory, which is a user facility supported by the US DOE BES. M.C. is supported by the US DOE BES,

Chemical Sciences, Geosciences, and Biosciences Division, Catalysis Science Program. All DFT calculations were performed on the IBM BlueGene/Q supercomputer with support from the Southern Ontario Smart Computing Innovation Platform (SOSCIP) and Niagara supercomputer at the SciNet HPC Consortium. SOSCIP is funded by the Federal Economic Development Agency of Southern Ontario, the Province of Ontario, IBM Canada Ltd., Ontario Centres of Excellence, Mitacs and 15 Ontario academic member institutions. SciNet is funded by the Canada Foundation for Innovation, the Government of Ontario, Ontario Research Fund - Research Excellence and the University of Toronto. We thank T. Wu, Y. Z. Finfrock, L. Ma and G. Sterbinsky for technical support at the 9BM beamline of the Advanced Photon Source. D.S. acknowledges the NSERC E. W. R. Steacie Memorial Fellowship. J.L. acknowledges the Banting Postdoctoral Fellowships Program. We thank M. Wei from the University of Toronto for discussions and help.

Author contributions

E.H.S. supervised the project. X.W. designed and carried out the experiments, analysed the data and wrote the paper. Z.W. carried out DFT simulations and wrote the corresponding section. X.W. and A.O. carried out the MEA measurements. D.-H.N., Y.-S.L., F.L., Y.L. and S.-F.H. performed synchrotron X-ray spectroscopy measurements. Z.C. and M.C. conducted the preparation and characterization of STEM/TEM ultrathin slices of catalyst. B.C., J.T., J.Y.H. and B.S. conducted TEM characterizations. Y.W. and J.T. performed part of the SEM characterizations. J.W., A.P. and P.T. carried out XPS measurements. A.R.K. and L.J.R. carried out the WAXS measurements and analysed the WAXS data. C.M. carried out the local species concentration modelling. C.M.G. and C.P.O. provided help with the MEA measurements. F.P.G.d.A., C.-T.D., Y.C.L., J.L., T.-T.Z., M.L., Y.M., A.X., B. Stephen, B. Sun, A.H.I., S.O.K. and D.S. assisted with the discussions. A.R.K. is a guest researcher. All authors discussed the results and contributed to the preparation of the manuscript.

Competing interests

A patent application regarding confined electrocatalysis for CO₂-to-ethanol is in preparation.

Additional information

Supplementary information is available for this paper at <https://doi.org/10.1038/s41560-020-0607-8>.

Correspondence and requests for materials should be addressed to E.H.S.

Reprints and permissions information is available at www.nature.com/reprints.

Publisher's note Springer Nature remains neutral with regard to jurisdictional claims in published maps and institutional affiliations.

© The Author(s), under exclusive licence to Springer Nature Limited 2020